High-resolution ground-based coronagraphy using image-motion compensation

D. A. Golimowski, M. Clampin, S. T. Durrance, and R. H. Barkhouser

The first results of a new approach to ground-based stellar coronagraphy are reported. A coronagraph has been equipped with an image-motion compensation system for the stabilization of the telescope field, permitting both improved image resolution and contrast at optical wavelengths. By stopping the telescope aperture D to $\sim 4\ r_0$, where r_0 is Fried's parameter, the maximum attainable resolution gain factor of 2.2 was achieved. Gains measured for $D/r_0 > 14$ were below the theoretical value of 1.3 theory and were indicative of centroid anisoplanatism, a small spatial coherence outer scale, or both. These effects are also evidenced by diminished power at low frequencies in the power spectrum of image motion over the full telescope aperture. A comparison of stabilized and unstabilized images shows that this coronagraph may detect circumstellar objects 2 magnitudes fainter than those detectable with a conventional coronagraph.

Key words: Adaptive optics, image-motion compensation, coronagraphy.

Introduction

The angular resolution of most ground-based optical telescopes is ultimately determined by the effects of atmospheric turbulence rather than the quality of the telescope optics. Incoming wave fronts from astronomical sources are distorted by refractive-index variations caused by random temperature and humidity fluctuations within the turbulent atmospheric layers. Phase shifts along the wave front produce blurring and motion of the astronomical image; the degrees of each depend on the scale of the turbulence and the size of the telescope aperture. For long-exposure images, the cumulative effect of these wave-front distortions is the degradation of the telescope's point-spread function from an Airy diffraction pattern to a broader quasi-Gaussian profile.[1] For smaller telescopes ($\lesssim$ 1.0 m at optical wavelengths), image motion resulting from wave-front tilt fluctuations provides the larger contribution to this image degradation, whereas blurring caused by higher-order wave-front aberrations dominates for larger apertures. The effect of atmospheric turbulence on image quality is commonly termed seeing and is typically characterized by the FWHM of the stellar profile. Seeing causes a significant loss of angular resolution and imaging sensitivity in ground-based astronomical observations; e.g., optical seeing conditions of 1 arcsec produce stellar images 10 to 40 times larger than those obtained with diffraction-limited 1- to 4-m aperture telescopes, respectively.

Many techniques have been employed in the effort to overcome the effects of the atmosphere on image quality, such as the postimaging-reconstruction methods of maximum entropy[2] and speckle imaging.[3,4] In the last decade, much attention has been given to real-time correction for seeing through the introduction of adaptive optics into the optical path.[5–7] An adaptive-optics system consists of a wave-front sensor and a deformable mirror operating in a closed-loop mode at rates appropriate for the time scale of the turbulence. Such a system not only corrects for atmospheric effects, but also compensates for aberrations induced by the telescope optics themselves.

An imaging technique that would benefit from the use of adaptive optics is stellar coronagraphy. The coronagraph was first employed by Lyot[8] in 1934 to observe the solar corona. Since then stellar coronagraphs have been successfully used to image faint material around bright stars, which is undetectable through direct-imaging techniques. The discovery of a protoplanetary disk about the star β Pictoris with a coronagraph[9] has inspired the Johns Hopkins University (JHU) to develop a coronagraph incorporating adaptive optics to conduct a full survey of circumstellar disk candidates with nearly diffraction-limited

The authors are with the Center for Astrophysical Sciences, Department of Physics and Astronomy, The Johns Hopkins University, Baltimore, Maryland 21218.

Received 01/09/92.
0003-6935/92/224405-12$05.00/0.

resolution at optical and near-infrared wavelengths. This combination of a coronagraph and adaptive optics would also permit the use of smaller occulting masks, thereby allowing one to image closer to the star. For β Pictoris, confirmation of a hypothesized clear zone within 30 astronomical units of the star, where planets may be accreting, should be possible with this instrument.

The present configuration of the JHU adaptive-optics coronagraph (AOC) employs an image-motion compensation system that is based on a quadrant-CCD detector and a piezoelectrically driven tip–tilt mirror to correct the effects of wave-front tilt across the telescope aperture. Thus, the AOC currently contains a partially adaptive optics system that removes only the lowest degree of image aberration. Ultimately, the AOC will incorporate a fully adaptive system, comprising the tip–tilt mirror, an electrostatically deformable membrane mirror for phase-error correction, and a wave-front curvature sensor of the type described by Roddier.[10] The partially adaptive instrument has been site tested at the European Southern Observatory (ESO) and at the Las Campanas Observatory. In this paper we present the results of these tests, which to our knowledge include the largest improvements in the angular resolution of optical images reported to date. A comparison of these results with the theory of atmospherically induced image motion shows that the AOC effectively removes this component of image distortion for apertures $\lesssim$ 1 m. The utility of the AOC in performing observations of the circumstellar environment of bright stars is also demonstrated.

Image-Motion Compensation

The effects of atmospheric turbulence on image quality have been reviewed by Roddier.[11] The spatial spectrum of the turbulence responsible for image degradation obeys Kolmogorov statistics, provided that the spatial frequencies f lie within the inertial range

$$l_0 \ll \frac{1}{f} \ll L_0, \tag{1}$$

where l_0 and L_0 are the inner and outer scales of the turbulence, respectively. The inner scale, defined as the length at which the mechanism of kinetic-energy dissipation changes from turbulent breakup to frictional heating, is $\lesssim$ 1 cm for all heights.[11] The outer scale reflects the size of the largest eddies that can be supported by the energy of the turbulent motion. In the troposphere, L_0 is generally thought to be of the order of the thickness of the turbulent layer, ranging from a few decameters to $\sim$ 100 meters.[11,12] Near the ground, L_0 is of the order of the height above the ground.[11] Recent reports based on *in situ* measurements of the atmospheric pressure, temperature, and refractive-index profiles have shown a systematic altitude dependence of L_0, with an upper limit for L_0 above 1 km of $\sim$ 5 m.[13,14] Thus, for telescope apertures $\lesssim$ 5 m, image motion arising from fluctuations of the average wave-front tilt across the aperature may be considered the result of a nearly Kolmogorov spectrum of turbulence filtered by the telescope aperture D and the outer scale L_0.

The spatial coherence of the distorted wave front is typically characterized by Fried's parameter r_0, which at zenith is given by[11]

$$r_0^{-5/3} = 16.70\lambda^{-2} \int_0^\infty dh C_N^2(h), \tag{2}$$

where λ is the wavelength of light, h is the height above the ground, and $C_N^2(h)$ is the refractive-index structure constant. For given seeing conditions, r_0 corresponds to the aperture size below which the short-exposure image resolution is diffraction limited and above which it is seeing limited. The angular diameter (FWHM) of the seeing-degraded long-exposure image is related to r_0 by[15]

$$\theta = 0.976 \left(\frac{\lambda}{r_0}\right) \tag{3}$$

and varies with wavelength as $\lambda^{-1/5}$. The variance of the wave-front tilt with respect to the plane of the telescope aperture has been expressed as[11]

$$\sigma^2 \propto \int_0^\infty dh C_N^2(h) \int_{L_0(h)^{-1}}^{D^{-1}} df f^{-2/3}, \tag{4}$$

where the altitude dependence of L_0 is shown explicitly. Performing the integration over f and substituting Eq. (2) yields

$$\sigma^2 \simeq 0.36\lambda^2 r_0^{-5/3}[D^{-1/3} - \mathscr{L}_0^{-1/3}], \tag{5}$$

where $\mathscr{L}_0$ is the spatial coherence outer scale[14] defined as

$$\mathscr{L}_0^{-1/3} = \frac{\int_0^\infty dh L_0(h)^{-1/3} C_N^2(h)}{\int_0^\infty dh C_N^2(h)}, \tag{6}$$

and the constant of proportionality has been inserted to provide agreement with more rigorous derivations of σ^2 for an infinite outer scale.[16]

Borgnino[14] has introduced $\mathscr{L}_0$ as an estimator of the distance at which the structure function of phase fluctuations saturates (i.e., the self-coherence of the phase is zero). Relations (5) and (6) indicate that values of $\mathscr{L}_0$ obtained from simultaneous ground-based measurements of r_0 and σ^2 cannot be directly compared with *in situ* measurements of L_0 unless a single layer of homogeneous turbulence is assumed. However, $\mathscr{L}_0$ is a useful parameter for estimating the degree to which L_0 reduces the amount of image motion otherwise expected from fully developed Kolmogorov turbulence. To illustrate this point, let σ_∞^2 be the wave-front tilt variance as $L_0 \to \infty$ for all h.

Then relation (5) may be expressed as

$$\sigma^2 \simeq \left[1 - \left(\frac{D}{\mathscr{L}_0}\right)^{1/3}\right] \sigma_\infty^2. \quad (7)$$

Using Borgnino's[14] overestimate of $\mathscr{L}_0 = 7.67$ m, we find that the rms image motion recorded with a 2-m telescope would be $\sim$ 60% of that expected for fully developed turbulence. Thus, failure to account for such a finite outer scale would lead to an overestimation of the role of image motion in image degradation.

(It should be noted that relation (4) assumes a Kolmogorov spectrum of turbulence for all spatial scales, which is in violation of relation (1). Less image motion is expected for $f \sim L_0(h)^{-1}$ than is predicted by Kolmogorov theory. Further, relation (4) assumes that contributions to the image-motion power spectrum from scale lengths less than D are zero as a result of spatial averaging over the aperture. Having computed nonnegligible increases in the Strehl ratios of short-exposure images over those of long-exposure images for values of D/L_0 as much as 4, Valley[17] has shown that this assumption is only approximate for a single layer of homogeneous turbulence. Thus, $\mathscr{L}_0$ must be considered a diagnostic measurement, not an accurate measurement, of the effect of L_0 on image motion.)

The time between wave-front tilt fluctuations within which an adaptive correction must be applied is determined by the flow of frozen-in turbulence across the telescope aperture:

$$\tau \simeq \frac{D}{\bar{v}}, \quad (8)$$

where $\bar{v}$ is the average velocity of the turbulent layers. The angular extent of the sky over which image-motion compensation is effective, or the correlation angle, is by geometry

$$\Omega \simeq \frac{D}{\bar{h}}, \quad (9)$$

where $\bar{h}$ is the average height of the turbulent layers. For typical values of $\bar{h}$, a correlation angle of 1.5 arcmin is possible on a 2-m telescope, which reflects a factor of D/r_0 increase over the correlation (or isoplanatic) angle for fully adaptive systems.

To evaluate the benefits of image-motion compensation, Fried[18] has calculated the expected improvement in image resolution for short exposures as a function of D/r_0. These calculations apply equally well to the expected improvement in the resolution of long-exposure images obtained with real-time wave-front tilt correction by means of a tip–tilt mirror. The principal advantage of real-time tilt correction over *a posteriori* shift-and-add processing of short-exposure images is the enhanced ratio of signal to noise in the resulting image, which improves the chances of resolving faint objects with a noise-limited detector. Another advantage that is important for stellar coronagraphy is the ability to use smaller occulting masks, permitting high-resolution imaging closer to the star.

The expected gains in resolution using image-motion compensation for various values of D/r_0 are represented by the dashed curve in Fig. 1. These gains have been computed from Fried's tabulations of long- and short-exposure image resolutions[18]; however, our resolution pertains to the physically measurable image spread and is therefore inversely proportional to the square root of Fried's resolution.[11] Although Fried based his calculations on the inaccurate assumption that wave-front tilt is statistically independent from higher-order wave-front aberrations, his resolution gains have been characterized as being low by no more than 10% at peak gain.[19,20] For lack of better-tabulated resolution values, we refer to Fig. 1 with appropriate caution. When $D/r_0 \sim 3$–4, the image may be sharpened by a factor of $\sim$ 2. However, as D/r_0 increases the resolution gain rapidly decreases, because spatial averaging of the tilt contributions from smaller scales of turbulence produces little overall tilt across the telescope aperture. When $D/r_0 < 3$, the telescope's diffraction limit becomes comparable with the size of the blurred image, so the gain achieved by image-motion compensation again decreases. The favorable regime for image-motion compensation is $D/r_0 \sim 1$–10, where gains between 1.4 and 2.1 may be achieved. Note that these expected values also require $D \ll \mathscr{L}_0$ and are diminished if the condition is not satisfied.

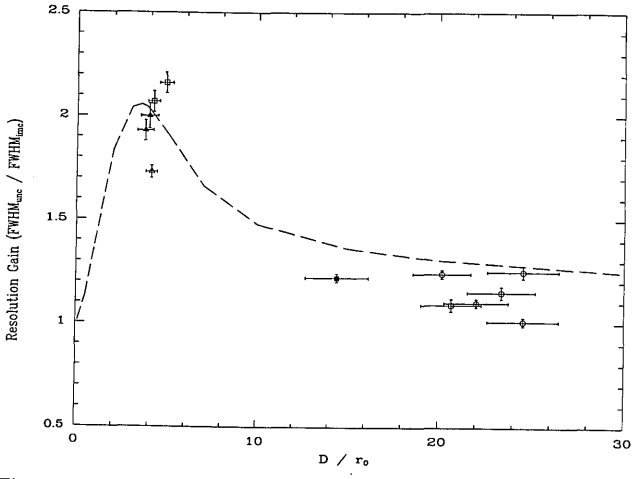

Fig. 1. The gain in angular resolution when the effects of wave-front tilt are removed. The dashed curve depicts the ratio of Fried's calculated short- and long-exposure resolutions for various values of D/r_0. The symbols represent the gains measured for AOC images obtained with the following telescope apertures: ESO 2.2-m MPI telescope at full aperture (open circles), ESO 2.2-m MPI telescope stopped to 0.6 m (open squares), ESO 2.2-m MPI telescope stopped to 0.5 m (open triangle), 2.54-m DuPont telescope at full aperture (filled square), and the 2.54-m DuPont telescope stopped to 0.7 m (filled triangles). The error bars for each datum reflect the uncertainty in the measurements of the image FWHM's and the width of the filter bandpass.

The Adaptive-Optics Coronagraph

The AOC consists of two major components: an adaptive-optics system used to sense and correct wave-front distortion, and a stellar coronagraph used to search for faint circumstellar emission. An occulting mask is the element common to both components, serving to prevent the light of a bright star from entering the coronagraph and reflecting that light into the wave-front sensor. The present AOC incorporates only those elements necessary for image-motion compensation, but the instrument has been constructed to easily accommodate future elements that will render the AOC fully adaptive. A schematic of the AOC and its peripheral control system is shown in Fig. 2. Light from the focal plane of the telescope is collimated by lens L1 onto the flat mirrors M1 and M2. M1 will ultimately be replaced by the membrane mirror in the fully adaptive instrument. M2 is driven by three piezoelectric actuators designed to provide rapid tip–tilt adjustment for removing overall wave-front tilt. The tip–tilt mirror is manufactured by Burleigh Instruments, Inc. and is capable of operating at rates in excess of 1 kHz. The telescope focal plane is reimaged with unit magnification by lens L2 onto the occulting mask M3. This small mirrored disk reflects the light of the bright star into the image-motion compensation system, permitting only the light from the circumstellar region to pass to the imaging camera.

The Image-Motion Compensation System

The image-motion compensation system is used to stabilize a stellar image once it has been positioned behind the occulting mask. The system consists of a

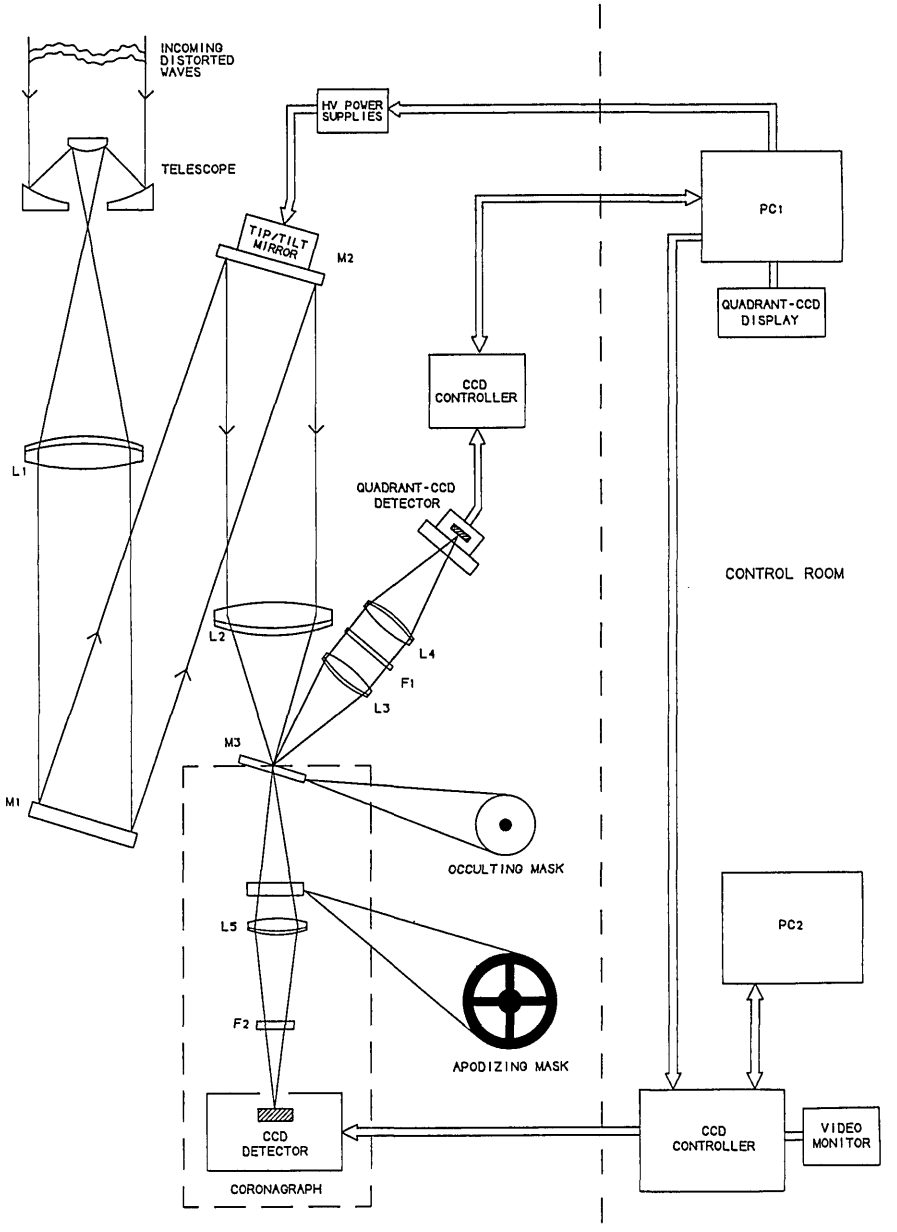

Fig. 2. Schematic of the JHU AOC configured for image-motion compensation: HV, high-voltage.

2×2 pixel quadrant-CCD detector, a control system based on an IBM-AT compatible personal computer (PC1), and the tip–tilt mirror. Lenses L3 and L4 reimage the star onto the quadrant-CCD, with L4 replaceable to provide a magnification suitable for the telescope plate scale. A neutral-density filter F1 may be inserted between L3 and L4 to prevent saturation of the detector. After each readout of the quadrant-CCD, the PC1 calculates the coordinates of the image centroid relative to the center of the quadrant-CCD. The PC1 then outputs voltage signals to the tip–tilt mirror necessary to return the image to the center position. The quadrant-CCD is mounted on a remotely controllable x–y translation stage to permit precise centering of the star behind the occulting mask. The closed-loop system typically operates at a sampling frequency of 100 Hz, with a 1.2 ms lag between each readout of the quadrant-CCD and the corresponding adjustment of the tip–tilt mirror. A detailed discussion of the characteristics of the quadrant-CCD detector has been given by Clampin *et al.*[21]; therefore, only a brief description follows.

Because the frequency spectrum of the image motion may contain significant power out to ~ 50 Hz for smaller-aperture telescopes, closed-loop correction rates up to ~ 300 Hz may be required to sample the turbulence well. Thus a sensor capable of detecting the motion of a point source at such rates is needed. We selected the quadrant-CCD built by Tektronix for an investigation of alternative fine-guidance sensors for the Hubble Space Telescope.[22] The quadrant-CCD is a three-phase front-side-illuminated device having four 100 μm $\times$ 100μm pixels that can be read out through a serial register at rates in excess of 1 kHz. The device has a peak quantum efficiency of ~40% and a read noise of approximately 10 e^- rms. Cooling to -40 °C is accomplished by using a four-stage thermoelectric stack and yields negligible dark noise for integration times < 100 ms. The performance of the quadrant-CCD is determined by analyses of the x and y transfer functions and of the noise equivalent angle (NEA). Each transfer function reflects the response of the quadrant-CCD as an appropriately sized image is slewed across the chip. The region of each transfer function in which the response changes polarity has been shown to be quite linear and encompasses the expected range of image motion.[21] These characteristics make the quadrant-CCD extremely suitable for image-motion sensing. The NEA is a measure of the uncertainty in the image centroid arising from photon and read noise. It is defined as

$$\mathrm{NEA} = \frac{1}{T \times S/N}, \tag{10}$$

where T is the slope of the transfer function and S/N is the signal-to-noise ratio of the image. The system's limiting magnitude is determined from the point at which the NEA becomes comparable with the image-motion amplitude measured by the system. For the ESO 2.2-m Max Planck Institute (MPI) telescope, the NEA becomes appreciable at visible magnitudes of 10–11 for 10-ms exposures. This limiting magnitude could be extended by improving the quadrant-CCD quantum efficiency through thinning and antireflection coating the device, but it is quite suitable for our current scientific objectives.

The controller electronics for the quadrant-CCD are a modified version of the Palomar Observatory system described in detail by Gunn *et al.*[23] PC1 controls the quadrant-CCD system through a direct-memory access card, which interfaces to the quadrant-CCD controller electronics. Because it takes 1.2 ms to read the chip, compute the centroid, and output the appropriate correction signals to the tip–tilt mirror, CCD integration times > 2 ms are required for the operation of the feedback loop. During the computation of the centroid, the pixel values are thresholded to discriminate cosmic-ray events. If the rms image motion exceeds a predefined value, the imaging camera's shutter is closed, permitting short periods of bad seeing to be rejected in real time and thereby improving the quality of the final image. For 1- to 2-m telescopes, typical integration times of 10–20 ms are used to sample the image-motion power spectrum adequately. During operation of the feedback loop, the PC1 software provides a real-time graphic display of the centroids and image-motion statistics. Image-centroid data may also be stored for subsequent power-spectrum analysis.

The Coronagraph

The coronagraph section of the AOC is shown contained within the dashed box in Fig. 2. The occulting mask M3, located at the reimaged telescope focal plane, marks the entrance to the coronagraph. It is mounted on a remotely controllable x–y translation stage to permit precise positioning anywhere in the field. The occulting mask is made by evaporating aluminum through a small pinhole onto a clear glass window. Masks ranging in size from 1 to 6 arcsec (depending on the telescope plate scale) have been made and are easily interchangeable with evolving seeing conditions. The occulting mask may be replaced with a beam splitter or dichroic to permit direct imaging and image-motion sensing of a single object.

An apodizing mask is placed at the plane of the reimaged telescope exit pupil following M3. This mask is a Lyot stop used to suppress the light diffracted by the telescope aperture and secondary mirror-support assembly. At the focal plane, such diffracted light from a bright star inhibits the detection of faint circumstellar emission. An apodizing mask that reduces the pupil radius by 20% will effectively reduce the diffracted light at the focal plane by more than an order of magnitude. The suppression of diffracted light, however, comes at the expense of a smaller effective aperture. This smaller aperture may present difficulties for the detection of faint circumstellar material with conventional corona-

graphs, but these difficulties are countered by the improved signal-to-noise ratio in the images obtained with the AOC.

Lens L5 reimages the circumstellar field onto the imaging camera with a magnification of ~ 6. The light is spectrally filtered by F2 for broad- or narrow-wavelength band imaging. The imaging camera system is manufactured by Photometrics Ltd. and employs a Thomson-CSF 384 × 576 pixel CCD. The CCD has a spectral range of 0.4–1.02 μm, with a peak quantum efficiency of 38% at 0.70 μm. The pixel size is 23 μm, which with the magnification from L5 provides for a well-sampled point-spread function. The format of the CCD has permitted fields of view of 20–60 arcsec, depending on the telescope plate scale. The read noize of 6 e^- and a dark count of <1 normal weight h^{-1} when the CCD is cooled to −120 °C are both adequate for the detection of faint circumstellar material.

Image acquisition and storage is controlled from PC2 through a general purpose interface bus to the CCD camera controller. Supporting software has been written to assist in observing tasks, such as target acquisition and telescope focusing. Once the target has been acquired, camera control is switched to PC1, which is part of the image-motion compensation system. As we described previously, PC1 suspends the exposure during periods of particularly bad seeing or errant telescope tracking. Once the exposure is completed, control is returned to PC2 for image storage.

Performance of the AOC

Demonstration of Image-Motion Compensation

Observations using the AOC were conducted during the nights of 24–30 May 1990 with the ESO 2.2-m MPI telescope at La Silla, Chile, and again during 1–6 December 1990 with the 2.54-m DuPont telescope at the Las Campanas Observatory in Chile. During the course of the scientific program (a survey of circumstellar disks around infrared excess stars), additional images were obtained to evaluate the image-motion compensation system. The telescopes are $f/8$ and $f/7.5$, respectively, both yielding a plate scale of 0.04 arcsec $pixel^{-1}$ at the imaging camera. Because the AOC is designed to sample diffraction-limited images adequately, the images were oversampled and suitable for high-precision-resolution comparisons. Further, the entire imaged field lay within the correlation region for image-motion compensation determined from relation (9). Observations of several stars were made with R-band ($\lambda_c \sim 650$ mm, $\Delta\lambda \sim 100$ nm) and I-band ($\lambda_c \sim 830$ nm, $\Delta\lambda \sim 200$ nm) filters, which were placed at the location marked F2 in Fig. 2. For each star, an exposure was taken with the image-motion compensation system operational; the exposure was immediately followed by another taken with the system off. A closed-loop sampling frequency of 100 Hz was used for all observations in which the image-motion compensation system was operational. The quadrant-CCD beam was only neutrally filtered, so the effective bandpass was determined by the CCD's spectral response over 500–900 nm. The stars were sufficiently bright to ensure that the quadrant-CCD NEA was negligible for each observation. The size of the stellar image at the quadrant CCD was limited by lens L4 to less than one pixel for 1 arcsec seeing conditions. This limitation guaranteed accurate computation of the image centroid. To investigate the system performance as a function of D/r_0, we made observations with the full 2.2-m and 2.54-m apertures and also with subapertures of 0.7, 0.6, and 0.5 m, which were obtained by inserting stops at the reimaged telescope exit pupil corresponding to the position of mirror M1. The maximum stop diameter was constrained by the dimensions of the unobscured region of the telescope primary mirror.

The results of the image-motion compensation test observations are summarized in Table 1. Columns 1–5 provide information concerning the object, date, filter, telescope aperture, and exposure time for each observation. For I Velorum and HR 394, which are visual binaries with respective separations of 7.2 and 5.0 arcsec, image-motion sensing was performed using the occulted brighter star, and resolution measurements were made on the fainter companion. Image-motion sensing and direct imaging of the remaining two stars, HR 7575 and μ PsA, were conductd using a beam splitter transmitting approximately 10% of the light to the coronagraph and 90% to the quadrant CCD. Columns 6 and 7 list the FWHM's of the image profiles in arcseconds for the uncorrected and image-motion corrected images, respectively. These values reflect the averages of the FWHM's measured along orthogonal CCD directions without removal of any contribution to the image spread from the telescope optics. Column 8 lists the resolution gain, defined as the ratio of the FWHM's of the uncorrected and corrected images, for each observation. Inspection of these gains shows that in all but one case an improvement in resolution was obtained. To our knowledge, the gain of 2.16 achieved with the ESO 2.2-m telescope stopped to 0.6 m is the highest yet

Table 1. Performance of the Image-Motion Compensation System

Object	Date	Filter	D (m)	Exposure time (s)	Uncorrected FWHM (arcsec)	Corrected FWHM (arcsec)	Gain
I Vel	5/25/90	R	2.2	120	1.20	0.97	1.24
I Vel	5/26/90	R	2.2	30	1.46	1.45	1.01
HR 7575	5/27/90	R	2.2	60	1.23	1.13	1.09
HR 7575	5/27/90	R	2.2	60	1.46	1.17	1.25
HR 7575	5/27/90	R	2.2	60	1.31	1.19	1.10
HR 7575	5/27/90	R	2.2	60	1.39	1.21	1.15
HR 7575	5/27/90	R	0.5	120	1.07	0.62	1.73
μ PsA	5/27/90	R	0.6	120	1.06	0.49	2.16
μ PsA	5/27/90	R	0.6	180	0.91	0.44	2.07
HR 394	12/7/90	I	2.54	60	0.95	0.78	1.22
HR 394	12/7/90	I	0.7	100	0.94	0.47	2.00
HR 394	12/7/90	I	0.7	100	0.89	0.46	1.93

reported for wave-front tilt correction at optical wavelengths.[24–27] The tests conducted with the 0.5-, 0.6-, and 0.7-m subapertures produced gains between 1.73 and 2.16, implying that $D/r_0 \sim 3$–4 and that the maximum resolution improvement predicted by Fried[18] was attained.

Profiles of the pair of uncorrected and corrected images of μ PsA with the measured gain of 2.16 are shown in Fig. 3. These profiles illustrate an improvement in the Strehl ratio (defined as the peak intensity of the aberrated image divided by the peak intensity of a diffraction-limited image) from 0.037 to 0.092. The corrected-image profile contains a sharp central peak and low-level wings that have the same angular extent as the seeing disk of the uncorrected image. These wings are typical of images obtained with partially adaptive optics systems in which there are an insufficient number of actuated mirror elements to correct for wave-front phase errors caused by small spatial scales of turbulence.[28]

The determination of r_0 from each uncorrected image is complicated by the uncertainty of the contributions to the image size from local facility (dome) seeing and the telescope optics. If facility seeing is ignored, the atmospherically degraded image size may be estimated by deconvolving in quadrature the telescope point-spread function from the uncorrected image. The corresponding value of r_0 may then be calculated using Eq. (3). Facility seeing generally cannot be ignored, however, so the resulting value of r_0 reflects the combined effects of turbulence caused by both the atmosphere and local thermal gradients.

Because the contribution of the telescope optics to the image spread was not measured during either observing period, r_0 has been estimated for each observation using the uncorrected-image FWHM's listed in Table 1. (The presence of the telescope component renders each computed value of r_0 an underestimate of the true value.) Each gain has been plotted against its respective value of D/r_0 in Fig. 1 to permit comparison with theory. The error bars for each datum reflect the uncertainty in the measurements of the image FWHM's and the width of the filter bandpass. For the observations made with the full aperture of each telescope (i.e., for $D/r_0 > 14$), the gains were lower than predicted. The effect of an underestimated value of r_0 on this result can be investigated. For the ESO 2.2-m telescope, Maaswinkel *et al.*[25] previously adopted a figure of 0.5 arcsec for the image size caused by the telescope optics at full aperture for zenith angles of 30 to 45°. Each observation conducted with the full 2.2-m aperture was done at a zenith angle within this range. When this value of the telescope component and an additional 0.04 arcsec (obtained from ray-tracing the AOC optics) are deconvolved from the FWHM of each uncorrected image, at most a 6% increase in the resolution gain is obtained. After computing the new values for r_0 based on the deconvolved image FWHM's, we find that the resulting values of D/r_0 are reduced by no more than 9%. These revisions are insufficient to alter significantly the location of the full 2.2-m aperture data with respect to the theoretical gain curve in Fig. 1. The same is probably true for the observation made with the full-aperture 2.54-m telescope. The data obtained with the telescope subapertures are scattered about the peak of the theoretical gain curve. Estimated changes in the gains and computed values of r_0 after deconvolution also affect the location of these data in Fig. 1 inconsequentially. However, as is discussed in Section 2, Fried's calculation of the maximum resolution gain is low by ~ 10%, implying that the peak of the curve shown in Fig. 1 should be higher by ~ 5%. The subaperture data, therefore, generally lie at or just below the predicted maximum gain obtainable through image-motion compensation.

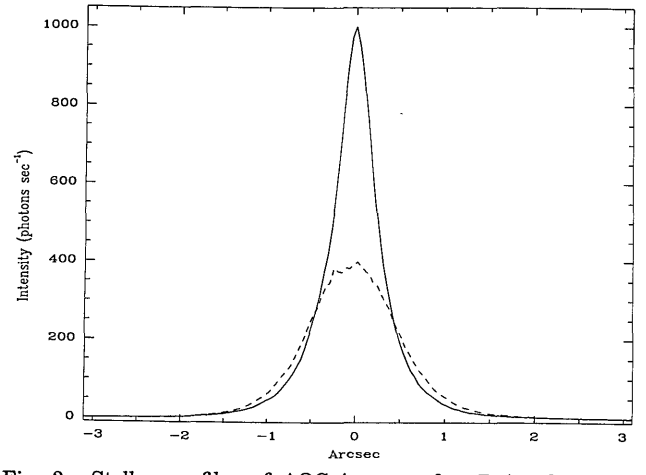

Fig. 3. Stellar profiles of AOC images of μ PsA taken with (solid curve) and without (dashed curve) image-motion compensation. The profiles reflect a reduction in image width from 1.06 to 0.49 arcsec and a 149% increase in the Strehl ratio. The images were obtained with the ESO 2.2-m MPI telescope stopped to 0.6 m.

Effects of Centroid Anisoplanatism and Finite $\mathscr{L}_0$

Although the resolution gains measured with the telescope subapertures matched theoretical expectation, those recorded with the full apertures fell short. Two possible explanations for this dichotomy are that (1) the effectiveness of the AOC image-motion compensation system is reduced for larger values of D/r_0, and (2) the role of image motion in the degradation of the full-aperture image is overestimated. Yura and Tavis[16] have addressed the first issue by investigating the ability of image-centroid tracking sensors to yield accurate overall wave-front tilt information. By comparing the variances of the wave-front tilt and the instantaneous image centroid, they concluded that the wave-front tilt angle is not completely correlated to the angular position of the image centroid. Although the discrepancy between the variances is small (the wave-front tilt variance is greater by ~ 7%, independent of D/r_0), this centroid anisoplanatism significantly reduces the improvement in the Strehl ratio expected from wave-front tilt correction for $D/r_0 \gtrsim 10$. According to Fig. 2 of Ref. 16, the Strehl

ratios of the corrected images obtained with the full 2.54-m and 2.2-m apertures should have been diminished by factors of 5 and 10, respectively. If the FWHM of each corrected image is assumed to be inversely proportional to its peak intensity (as in the case of a Gaussian profile), then the resolution gains recorded for these observations should also have been lower than expected by factors of 5 and 10. However, as we see in Fig. 1, only one of the gains measured with the full apertures was reduced so severely. It is possible that these gains primarily reflect the removal of image motion induced from nonatmospheric sources (such as telescope vibration); however, without proper characterization of such image motion, the effect of centroid anisoplanatism on AOC performance cannot be fully assessed.

The presence of centroid anisoplanatism does not preclude an investigation of reduced image motion for larger values of D/r_0. For the 0.6-m and 0.7-m subaperture observations, the measured gains of 1.93–2.16 imply that any reduction of image motion caused by a finite outer scale $\mathscr{L}_0$ must be small. (The lower gain recorded for the single 0.5-m subaperture test is not understood, but may be a result of aberrations induced by the off-axis aperture stop.) However, the effect of a finite $\mathscr{L}_0$ on the full-aperture gains may be evident, given Bornino's[14] estimate of $\mathscr{L}_0 <$ 7.67 m. This possibility can be checked by using simultaneous measurements of the image-centroid variance and r_0. During the 0.7-m and 2.54-m aperture observations of HR 394, the quadrant-CCD image centroid was recorded every 10 ms for a period of 10.24 s. The components of the image centroid measured along one axis of the quadrant-CCD for each aperture are shown in Figs 4(a) and 4(b). The dominant influence of high-frequency image motion on the long-exposure image spread for small telescope apertures is clearly shown. The centroid variances are 0.043 arcsec^2 and 0.013 arcsec^2 for the 0.7-m and 2.54-m aperture observations, respectively. The corresponding values of r_0 are obtained from the FWHM's of the uncorrected images of HR 394 recorded in Table 1. These images were recorded at positions sufficiently near zenith to validate their use in this

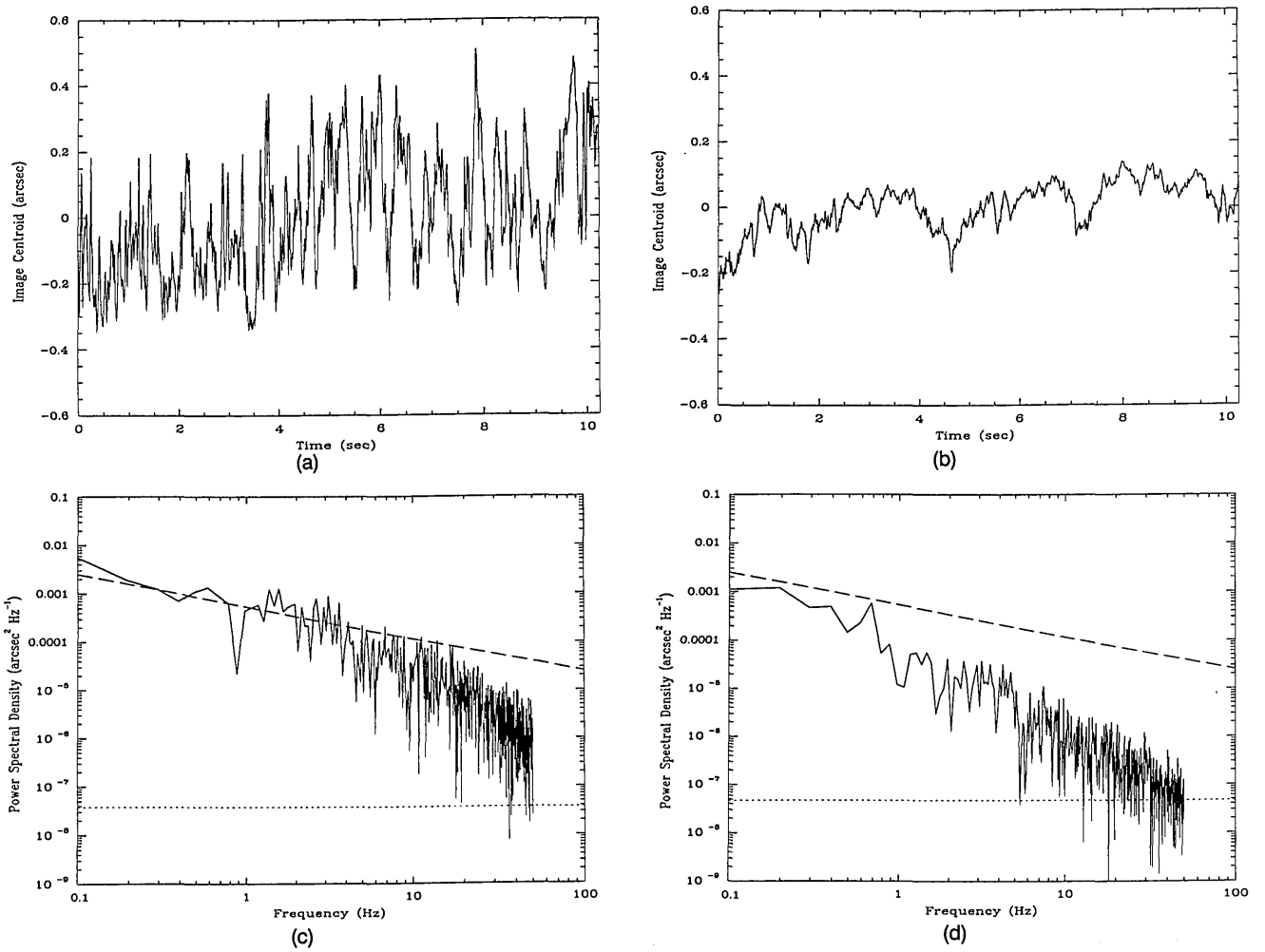

Fig. 4. Image motion of the star HR 394 recorded at 10-ms intervals for 10.24 s: (a), (b) Change in the image centroid for observations with the 0.7-m subaperture and the 2.54-m aperture, respectively; (c), (d) Computed one-sided power spectral density per unit time for the image centroids of (a) and (b). The long-dashed lines represent the $f^{-2/3}$ power law for Kolmogorov turbulence. The short-dashed lines indicate the level of the system noise.

analysis. Using relation (5), with an appropriate correction for centroid anisoplanatism, we estimate $\mathscr{L}_0$ to be 1.5 m from the subaperture data and 3.5 m from the full-aperture data. These estimates are quite disparate, and the value of $\mathscr{L}_0$ obtained for the 0.7-m subaperture is remarkably small given the resolution gains measured at that aperture.

It is evident from relation (5) that estimates of $\mathscr{L}_0$ are sensitive to errors in the measurements of σ^2, λ, and r_0. Because the image size at the quadrant CCD could not be precisely measured on the telescope, calibration of the image centroid for each aperture was performed using a laboratory-generated transfer curve obtained for the corresponding corrected-image size from Table 1. Assuming an uncertainty of ± 0.1 arcsec for the quadrant-CCD image size and employing the previously adopted uncertainties for λ and r_0, we find that the estimated uncertainties for the two values of $\mathscr{L}_0$ are ± 0.8 m and ± 0.7 m, respectively. These uncertainties are insufficient to bring the values of $\mathscr{L}_0$ for the two apertures into agreement. The remaining discrepancy may be attributed to the brevity of the centroid measurements compared with the uncorrected-image exposure time, which may have caused an undersampling of the low-frequency image motion. The disparity may also be a result of the added degradation of the long-exposure image from nonatmospheric sources. The long-exposure image size has been observed to be more sensitive than the image-motion variance to facility seeing[29] and telescope focus[30]; without proper characterization and removal of these components of the image spread, $\mathscr{L}_0$ will be underestimated. Telescope vibration must also be characterized and eliminated from the analysis. These factors were not measured during the observations, so the degree to which a finite $\mathscr{L}_0$ affected the full-aperture resolution gains remains ambiguous.

Power-Spectrum Analysis

The amount of image motion at a frequenty f can be determined through the computation of the one-sided power spectral density (PSD) per unit time of the image centroid. The PSD's for the centroids obtained with the 0.7- and 2.54-m apertures are shown in Figs. 4(c) and 4(d). Each PSD is normalized to the mean-squared centroid. For Kolmogorov turbulence, the PSD $\propto f^{-2/3}$, regardless of wind direction.[15] The dashed line in each figure represents the Kolmogorov power law scaled to best fit the low-frequency end of the 0.7-m aperture PSD. Despite the existence of a finite outer scale, the fit to the 0.7-m aperture PSD is quite good up to ~3.7 Hz. At this frequency the PSD drops considerably, reflecting the point at which spatial averaging over the aperture becomes significant. (The PSD ultimately falls to the level of the system noise, which is represented by the short-dashed line.) This turnover frequency, f_0, is related to the aperture size and to $v_\parallel$, which is the component of the wind velocity parallel to the direction of image motion, by[15]

$$f_0 \simeq 0.2 \frac{v_\parallel}{D}. \tag{11}$$

The wind speed along the given axis of the quadrant CCD for D = 0.7 m and f_0 = 3.7 Hz is approximately 13 m s^{-1}. Within the 0.1–3.7-Hz region of the 2.54-m aperture PSD the overall power is diminished, again revealing the combined effects of centroid anisoplanatism and a finite outer scale on low-frequency image motion. For this aperture $f_0 \sim 0.8$ Hz. From relation (11), we see that $v_\parallel \sim 10$ m/s^{-1}, which is in rough agreement with the subaperture case.

Comparison of Results

Several other systems designed to stabilize telescope images at optical wavelengths have been developed and tested, beginning in 1983 with the ISIS of Thompson and Ryerson.[24] More recent publications of performance tests have reported varying degrees of success. Maaswinkel *et al.*[25] have developed the DISCO adapter for the ESO 2.2-m MPI telescope, employing a fast mirror unit and an ICCD camera with electronics to calculate the image centroid. Operating at a 50-Hz correction rate and with the full telescope aperture, they reported an improvement in image resolution in 44% of their trials, with a best correction from 0.8 to 0.66 arcsec FWHM. Using an analysis of image centroids and uncorrected-image widths, they determined the outer scale of turbulence to be 5–20 m. (In retrospect, these values apply to an estimate of $\mathscr{L}_0$, not L_0.) The effects of centroid anisoplanatism were not considered.

Racine and McClure[26] have reported the results of a similar experiment at the 3.6-m Canada–France–Hawaii Telescope using HRCam, a system employing essentially the same elements for image-motion sensing and correction as the AOC. They achieved resolution improvements from 0.61 and 0.56 arcsec for the full aperture, and from 0.45 to 0.35 arcsec for a 1.2-m subaperture. They concluded that the telescope optics and facility seeing were responsible for the failure to achieve more significant improvements given the excellent seeing conditions ($r_0 \sim 40$ cm). In their analysis, Racine and McClure did not consider the effects of centroid anisoplanatism or a finite outer scale, which for a 3.6-m aperture may limit the role of image-motion compensation to the removal of some elements of facility seeing and telescope vibration.

Doel *et al.*[27] addressed the problem of a finite order scale for the 4.2-m William Herschel Telescope with the MARTINI instrument, which separately corrected for image motion across each of six 0.6-m subapertures. Image-motion sensing for all the subapertures was accomplished with a single photon-counting detector, and corrective signals were sent to six piezoelectrically driven mirrors located at a conjugate plane of the turbulent layer. The system permitted comparison of postexposure-sharpened images constructed from photon-arrival data with real-time

sharpened images recorded by the detector for each of the six subapertures. From an uncorrected-image FWHM of 0.6 arcsec, Doel *et al.* reported a best real-time correction of 0.35 arcsec (a resolution gain of 1.7) and a best postexposure reconstruction of 0.25 arcsec. The failure to achieve maximal correction in real time was attributed to unrefined mirror-positioning algorithms.

Coronagraphic Performance

The performance of a coronagraph is assessed by its ability to image an object of low surface brightness in the proximity of a comparatively bright star. The degree to which a coronagraph can limit the effects of diffracted and scattered light at the focal plane governs this performance. As is discussed in Section 3, suppression of light diffracted by the telescope aperture and secondary-mirror support assembly is accomplished by placing an apodizing mask at a location of the reimaged exit pupil within the AOC. Because the location of this diffracted light at the pupil plane is unaffected by wave-front tilt, image-motion compensation does not improve the efficiency of pupil plane apodization over that of conventional coronagraphs. For all the observations described above, diffracted light was satisfactorally suppressed using apodizing masks that reduced the effective telescope aperture by no more than 30%.

Image-motion compensation does, however, enhance coronagraphic performance by reducing the amount of light scattered into the outer regions of the seeing disk. This enhancement affords two advantages when imaging with the AOC instead of a conventional coronagraph. First, for a given exposure length (determined, e.g., by the saturation of the imaging detector) a smaller occulting mask may be used, thereby exposing regions closer to the bright central star. This point is illustrated by again examining the stellar profiles shown in Fig. 3. To occult the region of the uncorrected image with pixel intensities greater than 100 photons s^{-1} would require a mask with a diameter of 1.6 arsec. To do the same with the corrected image would require a 1.4 arcsec mask. Although this reduction in mask size is modest (even for these images obtained with optimal D/r_0), it does predict a greater benefit when higher-order aberrations are corrected by the fully adaptive AOC.

The second advantage of coronagraphic imaging with the AOC is improved contrast in the circumstellar region. Image stabilization and reduction of scattered light together result in a much-enhanced ratio of signal from the circumstellar material to photon noise from the occulted star. Consequently, the brightness limit for the detection of a faint object near the occulted star (after proper subtraction of the occulted stellar profile) is lowered. Figure 5 shows the R-band magnitude detection limit for a hypothetical star as a function of distance from the $R = 4.45$ magnitude star μ PsA. The upper and lower curves are based, respectively, on the radially averaged profiles of the uncorrected and corrected 180-s exposures of μ PsA recorded in Table 1. The detection limit at a given distance was defined by the point at which the peak of the hypothetical star profile equalled twice the photon noise of the μ PsA image. The hypothetical star image was given the same Strehl ratio as the corresponding image of μ PsA. Figure 5 shows that the AOC may reveal stellar sources up to 2 magnitudes fainter than those detectable with a conventional coronagraph throughout the immediate circumstellar environment.

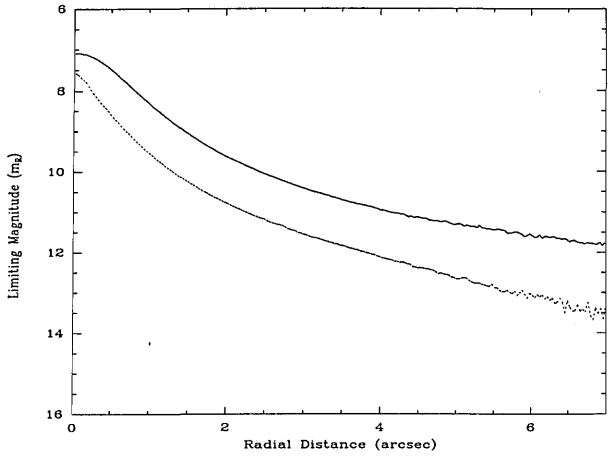

Fig. 5. Limiting R-band magnitude for detection of a hypothetical star as a function of distance from μ PsA. The curves are based upon radial averages of the 180-s exposures listed in Table 1. The solid curve represents the uncorrected (conventional coronagraph) case, whereas the dashed curve represents the image-motion corrected (AOC) case; μ PsA itself has an R magnitude of 4.45.

Three-dimensional surface plots of actual coronagraphic images, which give an exaggerated demonstration of the improved image contrast obtainable with the AOC, are shown in Figs. 6(a) and 6(b). The occulted star in each figure is ϵ Sagittarii, a B-type star with a visual magnitude of 1.85. The observations of ϵ Sgr were conducted at ESO as part of our survey of infrared excess stars and other circumstellar disk candidates.[31] Several 60-s exposures were obtained using the 0.6-m subaperture of the 2.2-m MPI telescope and a 4.7-arcsec occulting mask. Such a large mask was necessary because of the brightness of ϵ Sgr and the less-than-favorable seeing conditions. Figure 6(a) shows the surface plot of the uncorrected image of ϵ Sgr. Inspection of the halo of light surrounding the occulting mask shows that the mask was well centered on the star and suggests the presence of an unresolved feature at the edge of the mask. Figure 6(b) shows the corrected image of ϵ Sgr. This plot reveals the unresolved feature to be a star with a visual magnitude of ~ 8. This star, whether a companion to ϵ Sgr or a field star, is a likely cause of the measured infrared excess of ϵ Sgr. Further analysis of these images will be reported in an astronomical journal.

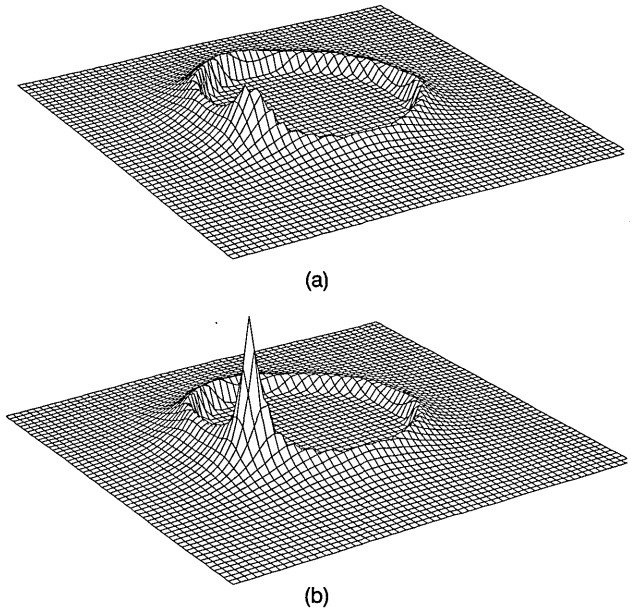

Fig. 6. Three-dimensional surface plots of AOC images of the infrared-excess star ϵ Sgr, obtained with the ESO 2.2-m MPI telescope stopped to 0.6 m and a 4.7-arcsec occulting mask. (a) Plot of the uncorrected image, showing an unresolved feature at the edge of the occulting mask. (b) The corrected image, which reveals the feature to be a star and a likely cause of the measured infrared excess. The two images illustrate the improved contrast in the circumstellar region obtainable with the AOC.

Concluding Remarks

Through successful implementation of an image-motion compensation system, the AOC has demonstrated significant improvement in the angular resolution and contrast of coronagraphic images. Performance tests under mediocre seeing conditions (0.9–1.5 arcsec) showed maximal resolution gains when $D/r_0 \sim 3$–4, which is in accordance with theoretical predictions. Tests conducted for $D/r_0 > 14$ resulted in gains lower than those predicted. The latter results, together with an analysis of short-exposure image-centroid data, indicate that (1) centroid anisoplanatism may indeed restrict the effectiveness of centroid trackers as wave-front tilt sensors for large values of D/r_0, and (2) the role of image motion in the degradation of long-exposure images for $D \gtrsim 2$ m may be smaller than expected under conditions of fully developed Kolmogorov turbulence.

Because centroid anisoplanatism and a finite outer scale together reduce the effectiveness of image-motion compensation for intermediate-size telescopes, such correction is most beneficial for apertures less than 2 m. In particular, 1-m-class telescopes based at good sites may achieve 0.3–0.4 arcsec images during subarcsecond seeing conditions with a relatively small investment in technology. The use of image-motion compensation for large apertures, however, may be feasible for the next generation of new technology telescopes, for which the telescope-tracking specifications preclude the use of traditional autoguiding systems. In such cases, fine guidance with a tip–tilt mirror would offer an effective alternative to an autoguider, thereby permitting optimum telescope performance. Although image-motion compensation at optical wavelengths is generally not well suited for telescope apertures greater than 2 m, such correction at near-infrared wavelengths (1.0–5.0 μm) is quite appropriate. At these wavelengths r_0 typically ranges from 30–360 cm, and values of D/r_0 favorable for optimal image-motion compensation are available even for 4-m-class telescopes.

The authors thank the Seaver Institute for its support of adaptive-optics development at The Johns Hopkins University. We are grateful to the observations of the Carnegie Institution of Washington for providing observing time at Las Campanas as well as to the observatory staff for its dedicated assistance. Observing time at the ESO 2.2-m MPI telescope was awarded by the Max Planck Institute in collaboration with F. Paresce and J. Staude. Finally, we acknowledge the enthusiastic support of adaptive-optics development at The Johns Hopkins University by the Center for Astrophysical Sciences. This paper is based on data obtained at the ESO and the Las Campanas Observatory.

References

1. I. R. King, "The profile of a star image," Publ. Astron. Soc. Pac. **83,** 199–201 (1971).
2. I. N. Evans, H. C. Ford, and X. Hui, "Maximum entropy deconvolution of the jet of 3C 273," Astrophys. J. **347,** 68–73 (1989).
3. P. Nisenson, "Speckle imaging with the PAPA detector and the Knox-Thompson algorithm," in *Proceedings of the NATO ASI Diffraction Limited Imaging with Very Large Telescopes,* D. M. Alloin and J. P. Mariotti, eds. (Kluwer, Dordrecht, The Netherlands, 1988), pp. 157–169.
4. G. Weigelt, "Speckle masking, speckle spectroscopy and optical aperture synthesis," in *Proceedings of the NATO ASI Diffraction Limited Imaging with Very Large Telescopes,* D. M. Alloin and J. P. Mariotti, eds. (Kluwer, Dordrecht, The Netherlands, 1988), pp. 191–200.
5. J. W. Hardy, J. E. Lefebvre, and C. L. Koliopoulos, "Real-time atmospheric compensation," J. Opt. Soc. Am. **67,** 360–369 (1977).
6. F. Merkle and J. M. Beckers, "Application of adaptive optics to astronomy," in *Active Telescope Systems,* F. J. Roddier, ed., Proc. Soc. Photo-Opt. Instrum. Eng. **1114,** 36–42 (1989).
7. G. Rousset, J. C. Fontanella, P. Kern, P. Gigan, F. Rigaut, P. Léna, C. Boyer, P. Jagourel, J. P. Gaffard, and F. Merkle, "First diffraction-limited astronomical images with adaptive optics," Astron. Astrophys. **230,** L29–L32 (1990).
8. B. Lyot, "A study of the solar corona and prominences without eclipses," Mon. Not. R. Astron. Soc. **99,** 580–594 (1939).
9. B. A. Smith and R. J. Terrile, "A circumstellar disk around β Pictoris," Science **226,** 1421–1424 (1984).
10. F. Roddier, "Curvature sensing and compensation: a new concept in adaptive optics," Appl. Opt. **27,** 1223–1225 (1988).
11. F. Roddier, "The effects of atmospheric turbulence in optical astronomy," in *Progress in Optics,* E. Wolf, ed. (North-Holland, Amsterdam, 1981), pp. 281–376.
12. N. J. Woolf, D. W. McCarthy, and J. R. P. Angel, "Performance of the Multiple Mirror Telescope (MMT) VII. Image shrinking in sub-arc second seeing at the MMT and 2.3 m telescopes," in *Advanced Technology Optical Telescopes I,* L. D.

Barr and G. Burbidge, eds., Proc. Soc. Photo-Opt. Instrum. Eng. **332,** 50–56 (1982).
13. C. E. Coulman, J. Vernin, Y. Coqueugniot, and J. L. Caccia, "Outer scale of turbulence appropriate to measuring refractive-index structure profiles," Appl. Opt. **27,** 155–160 (1988).
14. J. Borgnino, "Estimation of the spatial coherence outer scale relevant to long baseline interferometry and imaging in optical astronomy," Appl. Opt. **29,** 1863–1865 (1990).
15. H. M. Martin, "Image motion as a measure of seeing quality," Publ. Astron. Soc. Pac. **99,** 1360–1370 (1987).
16. H. T. Yura and M. T. Tavis, "Centroid anisoplanatism," J. Opt. Soc. Am. A **2,** 765–773 (1985).
17. G. C. Valley, "Long- and short-term Strehl ratios for turbulence with finite inner and outer scales," Appl. Opt. **18,** 984–987 (1979).
18. D. L. Fried, "Optical resolution through a randomly inhomogeneous medium for very long and very short exposures," J. Opt. Soc. Am. **56,** 1372–1379 (1966).
19. J. Y. Wang and J. K. Markey, "Modal compensation of atmospheric turbulence phase distortion," J. Opt. Soc. Am. **68,** 78–87 (1978).
20. N. Roddier, "Atmospheric wavefront simulation using Zernike polynomials," Opt. Eng. **29,** 1174–1180 (1990).
21. M. Clampin, S. T. Durrance, D. A. Golimowski, R. Barkhouser, J. A. Westphal, D. L. Heidtmann, and M. M. Blouke, "High speed quadrant-CCDs for adaptive optics," in *CCDs in Astronomy,* G. H. Jacoby, ed., Vol. 8 of Astronomical Society of the Pacific Conference Series (Astronomical Society of the Pacific, San Francisco, Calif., 1989), pp. 367–373.
22. W. G. Fastie, "Study of fine guidance systems for the Hubble Space Telescope," Rep. NAS8-35348 (National Aeronautics and Space Administration, Washington, D.C., 1989).
23. J. E. Gunn, E. B. Emory, F. H. Harris, and J. B. Oke, "The Palomar Observatory CCD camera," Publ. Astron. Soc. Pac. **99,** 518–534 (1987).
24. L. A. Thompson and H. R. Ryerson, "An active mirror image stabilizing instrument system (ISIS) for use on Mauna Kea," in *Instrumentation in Astronomy V,* A. Boksenberg and D. L. Crawford, eds., Proc. Soc. Photo-Opt. Instrum. Eng. **445,** 560–568 (1983).
25. F. Maaswinkel, F. Bortoletto, R. Buonanno, B. Buzzoni, S. D'Odorico, B. Gilli, G. Huster, and W. Nees, "Image stabilization with DISCO: results of first observing run," in *Proceedings of the ESO Conference on Very Large Telescopes and Their Instrumentation* (European Southern Observatory, Garching be: München, Germany, 1988), pp. 751–760.
26. R. Racine and R. D. McClure, "An image stabilization experiment at the Canada–France–Hawaii Telescope," Publ. Astron. Soc. Pac. **101,** 731–736 (1989).
27. A. P. Doel, C. N. Dunlop, J. V. Major, R. M. Myers, A. Purvis, and M. G. Thompson, "Stellar image stabilisation using piezo-driven active mirrors," in *Advanced Technology Optical Telescopes IV,* L. Barr, ed., Proc. Soc. Photo-Opt. Instrum. Eng. **1236,** 179–192 (1990).
28. R. C. Smithson and M. L. Peri, "Partial correction of astronomical images with active mirrors," J. Opt. Soc. Am. A **6,** 92–97 (1989).
29. F. Forbes, "Dome induced image motion," in *Advanced Technology Optical Telescopes I,* L. D. Barr and G. Burbridge, eds., Proc. Soc. Photo-Opt. Instrum. Eng. **332,** 185–192 (1982).
30. F. F. Forbes and N. J. Woolf, "Atmospheric turbulence effects on large telescope image motion and size," in *Advanced Technology Optical Telescopes II,* L. D. Barr ed. Proc. Soc. Photo-Opt. Instrum. Eng. **444,** 175–182 (1983).
31. J. Coté, "B and A type stars with unexpectedly large colour excesses at IRAS wavelengths," Astron. Astrophys. **181,** 77–84 (1987).